Journal of Inorganic Biochemistry 203 (2020) 110884

Contents lists available at ScienceDirect

Journal of Inorganic Biochemistry

journal homepage: www.elsevier.com/locate/jinorgbio

Structural modification of nanohydroxyapatite $Ca_{10}(PO_4)_6(OH)_2$ related to Eu^{3+} and Sr^{2+} ions doping and its spectroscopic and antimicrobial properties

Katarzyna Szyszka[a,*], Justyna Rewak-Soroczynska[a], Agata Dorotkiewicz-Jach[b], Karolina A. Ledwa[a], Agata Piecuch[b], Michael Giersig[c,d], Zuzanna Drulis-Kawa[b], Rafal J. Wiglusz[a,*]

[a] Institute of Low Temperature and Structure Research, PAS, Okolna 2, PL-50-422 Wroclaw, Poland
[b] Institute of Genetics and Microbiology, University of Wroclaw, Przybyszewskiego 63/77, 51-148 Wroclaw, Poland
[c] Freie Universität Berlin, Institute of Experimental Physics, Arnimallee 14, 14195 Berlin, Germany
[d] International Academy of Optoelectronics at Zhaoqing, South China Normal University, 526238, Guangdong, PR China

ARTICLE INFO

Keywords:
Spectroscopy
Apatite
Biomaterial
Europium
Strontium
Antibacterial activity

ABSTRACT

The Eu^{3+} and Sr^{2+} ions co-doped hydroxyapatite nanopowders ($Ca_{10}(PO_4)_6(OH)_2$) were synthesized *via* a precipitation method and post heat-treated at 500 °C. The concentration of Eu^{3+} ions was established in the range of 0.5–5 mol% to investigate the site occupancy preference. The concentration of Sr^{2+} ions was set at 5 mol%. The structural and morphological properties of the obtained materials were studied by an X-ray powder diffraction, a transmission electron microscopy techniques and infrared spectroscopy. As synthesized nanoparticles were in the range of 11–17 nm and annealed particles were in the range of 20–26 nm. The luminescence properties in dependence of the dopant concentration and applied temperature were investigated. The $^5D_0 \rightarrow {}^7F_0$ transition shown the abnormally strong intensity for annealed materials connected with the increase of covalency character of Eu^{3+}–O^{2-} bond, which arise as an effect of charge compensation mechanism. The Eu^{3+} ions occupied three possible crystallographic sites in these materials revealed in emission spectra: one Ca(1) site with C_3 symmetry and two Ca(2) sites with C_s symmetry arranged as *cis* and *trans* symmetry. The antibacterial properties of Eu^{3+} and Sr^{2+} ions doped and co-doped hydroxyapatite nanopowders were also determined against Gram-negative pathogens such as *Pseudomonas aeruginosa*, *Klebsiella pneumoniae* and *Escherichia coli*. Obtained results suggest that both europium and strontium ions may implement antibacterial properties for hydroxyapatites. In the most cases, better antibacterial effect we noticed for dopants at 5 mol% ratio. However, the effect is strongly species- and strain-dependent feature.

1. Introduction

Progressive loss of bones mineral density leads to changes in bone architecture and higher probability of fractures. A disease called osteoporosis is a serious public health problem of elderly people in western countries, which can be even worse in the future [1,2]. Unfortunately, human organism possesses merely a limited ability of autoregeneration of its major tissues and organs in the case when the tissue integrity has been deeply damaged [3]. Because of this, materials with stimulating capacity which can enhance the tissue regeneration are the next generation of biomaterials [4]. One of the most important and the best biomaterial is calcium hydroxyapatite (thereafter - HAp) which is similar to inorganic component of bones and teeth. Because of this similarity, hydroxyapatite is non-toxic for humans, bioactive and it is broadly used in medicine [5–9]. Nevertheless, the properties of hydroxyapatite have been still improved through obtaining appropriate grain size and morphology, adding some dopants such as Sr^{2+}, Mg^{2+}, Zn^{2+}, F^-, $CO_3{}^{2-}$, which are also naturally built into the human bone tissue, and achieve special role in homeostasis. Due to this, these doping agents can improve the biological response of an organism. Other ions such as Ag^+, Cu^{2+} and lanthanides can improve antibacterial properties of HAp or even enable bioimaging [5,10–15]. Strontium is a trace element in human body which influences the strength, healing, and microarchitecture of bones. Strontium ion stimulates bone formation,

* Corresponding authors.
E-mail addresses: K.Szyszka@intibs.pl (K. Szyszka), R.Wiglusz@intibs.pl (R.J. Wiglusz).

https://doi.org/10.1016/j.jinorgbio.2019.110884
Received 21 June 2019; Received in revised form 4 October 2019; Accepted 6 October 2019
Available online 22 October 2019

inhibits bone resorption and also improves bioactivity and biocompatibility of biomaterials [16–18]. Their positive impact on osteoporosis treatment was also observed [2,18,19]. The Sr^{2+} ions in the form of orally taken strontium ranelate have been used in osteoporosis therapy, but the bioavailability of this formulation is limited [2,20]. The incorporation of a small amount of Sr^{2+} directly into biomaterials can additionally support osteoporosis therapy.

Biomaterials incorporated into the human body should possess antibacterial properties as they are exposed to the bacterial colonization. During the operation procedures, the human organism is also vulnerable to the infections. Bacteria can easily develop a biofilm structure on implants and protect themselves from environmental conditions and human immune system. The infection developing at the site of implantation can spread further and cause serious life-threatening problems [21]. Therefore, the antibacterial properties of newly designed biomaterials are crucial for successful implantation. Nowadays, the application of antibiotics in preoperative prophylaxis becomes limited as the bacteria have developed multidrug resistance mechanisms. We are facing an urgent need for new antibacterials [22]. One of the possibilities is the incorporation of different cations, having a strong antibacterial effect, into the implanted biomaterials to prevent bacterial biofilm and infection development. Amongst them, europium and strontium depending on the concentration of ions possess documented antibacterial effects [23,24].

In this study, there have been investigated the preparation of the nanohydroxyapatite $Ca_{10}(PO_4)_6(OH)_2$ doped with Eu^{3+} and Sr^{2+} ions as structurally modified biomaterial to promote bone regeneration process (hydroxyapatite) and to enable bio-imaging (Eu^{3+}) with additional antibacterial properties (Eu^{3+} and Sr^{2+}) for theranostics application.

2. Experimental

2.1. Synthesis of the Eu^{3+}/Sr^{2+}:$Ca_{10}(PO_4)_6(OH)_2$ nanopowders

The nanocrystalline powders of the $Ca_{10}(PO_4)_6(OH)_2$ co-doped with Eu^{3+} and 5 mol% Sr^{2+} ions were synthesized by precipitation method. As starting substrates $CaCO_3$ (99.5% metals basis Alfa Aesar), $Sr(NO_3)_2$ (min. 99.0% Alfa Aesar), $NH_4H_2PO_4$ (≥99.0% Fluka), Eu_2O_3 (99.99% Alfa Aesar) and $NH_3{\cdot}H_2O$ (99% Avantor Poland) for pH regulation were used. The concentration of strontium ions has been set at 5 mol% and the concentration of the optically active europium ions has been established at 0.5, 1, 2 and 5 mol% in substitution of overall molar content of divalent cations as the following process. Separately, the stoichiometric amount of the $CaCO_3$, as well as Eu_2O_3, was digested in an excess of the HNO_3 (suprapure Merck) to receive water-soluble nitrates. The europium nitrates hydrates were re-crystallized three times in order to get rid of the HNO_3 excess and were dissolved in deionized water. Afterwards, calcium nitrates and europium nitrates were mixed together. Then the appropriate amounts of $NH_4H_2PO_4$ were added to previous mixture. The pH value of the dispersion was adjusted to 10 by ammonia. The suspensions were heated and stirred on stirring plate for 3 h. Finally, the obtained products were centrifuged, rinsed with deionized water several times and dried at 70 °C for 24 h. The materials were heat-treated at 500 °C per 3 h.

2.2. Materials characterization

The crystal phase purity of obtained materials was checked by the X-ray powder diffraction (XRPD) technique using a PANalytical X'Pert Pro X-ray diffractometer equipped with Ni-filtered Cu $K\alpha_1$ radiation ($K\alpha_1$ = 1.54060 Å, V = 40 kV, I = 30 mA). The experimental XRD patterns were compared with the standard from Inorganic Crystal Structure Database (ICSD - 180,315 [25]) to confirm the formation of apatite structure. High-resolution transmission electron microscopy (HRTEM) images were performed by using a Philips CM-20 SuperTwin microscope, operating at 200 kV. Sample for HRTEM was prepared by dispersing a small amount of specimen in methanol and putting a droplet of the suspension on a copper microscope gird covered with carbon. The morphology investigation and the mapping of the elements were done by a FEI Nova NanoSEM 230 scanning electron microscope (SEM) equipped with an energy-dispersive X-ray spectrometer (EDAX Genesis XM4) and operating at an acceleration voltage in the range 3.0–15.0 kV and spot 2.5–3.0.

A Nicolet iS50 Fourier Transform Infrared Spectroscopy (FT-IR Thermo Scientific) spectrometer equipped with an Automated Beamsplitter exchange system (iS50 ABX containing DLaTGS KBr detector), built-in all-reflective diamond attenuated total reflectance module (iS50 ATR), Thermo Scientific Polaris™ and HeNe laser as an IR radiation source were used to measure IR spectra. Polycrystalline mid-IR spectra were collected in the 4000–400 cm^{-1} range in KBr pellets and spectral resolution was set to 4 cm^{-1}.

The excitation spectra were measured using FLS980 Fluorescence Spectrometer (Edinburgh Instruments). A 450 W xenon lamp was used as an excitation source. The excitation of 300 mm focal length monochromator was in Czerny-Turner configuration. The excitation arm was supplied with holographic grating of 1800 lines/mm grating blazed at 250 nm. As a detector, a Hamamatsu R928P photomultiplier was used. All spectra were corrected according to the characteristics of the intensity of the excitation source. The emission and luminescence kinetics were recorded using Jobin-Yvon THR1000 monochromator equipped with Hamamatsu R928 photomultiplier and 1200 lines/mm grating blazed at 500 nm. A pulsed 266 nm line of YAG:Nd laser (3rd harmonic, λ_{exc} = 266 nm) was used as an excitation source. The spectral resolution was 0.1 nm. All the emission spectra were corrected to the detector sensitivity. The decay profiles were collected using a LeCroy WaveSurfer 400 MHz oscilloscope. The luminescence kinetics were recorded at 617 nm according to the most intense electric dipole transition ($^5D_0 \rightarrow {}^7F_2$).

2.3. Bacterial strains

Four reference strains of Gram-negative *Enterobacteriaceae*, from the American Type Culture Collection were used: *Klebsiella pneumoniae* ATCC 700603, *Escherichia coli* ATCC 11229, *Escherichia coli* ATCC 25922 and *Escherichia coli* ATCC 35218. Bacteria were stored at −70 °C in Trypticase Soy Broth (Becton Dickinson and Company, Cockeysville, MD, USA) supplemented with 20% glycerol.

2.4. Determination of antibacterial activity of Eu^{3+}/Sr^{2+}:$Ca_{10}(PO_4)_6(OH)_2$ nanopowders

The antimicrobial activity of the Eu^{3+}/Sr^{2+}:$Ca_{10}(PO_4)_6(OH)_2$ nanopowders was performed by the microdilution method according to EUCAST (The European Committee on Antimicrobial Susceptibility Testing) recommendations with previously described modifications [9,26]. The 100 μg/mL of $Ca_{10}(PO_4)_6(OH)_2$ un-doped, doped or co-doped with Eu^{3+} and Sr^{2+} in a saline were tested. Positive controls (100% survival rate) consisted of bacteria inoculated in a saline, whereas uninoculated nanopowders dilutions in saline were used as negative controls (sterility). Each assay was repeated in triplicate at three different times to ensure the reproducibility of results. The number of colony forming units (CFU/mL) was determined after the incubation at 37 °C for 20 h and compared to the positive control. The data values were expressed as mean ± SD and significant differences between variations (denoted $p < 0.001$) were found by means of the Snedecor-Fisher test using one-way ANOVA.

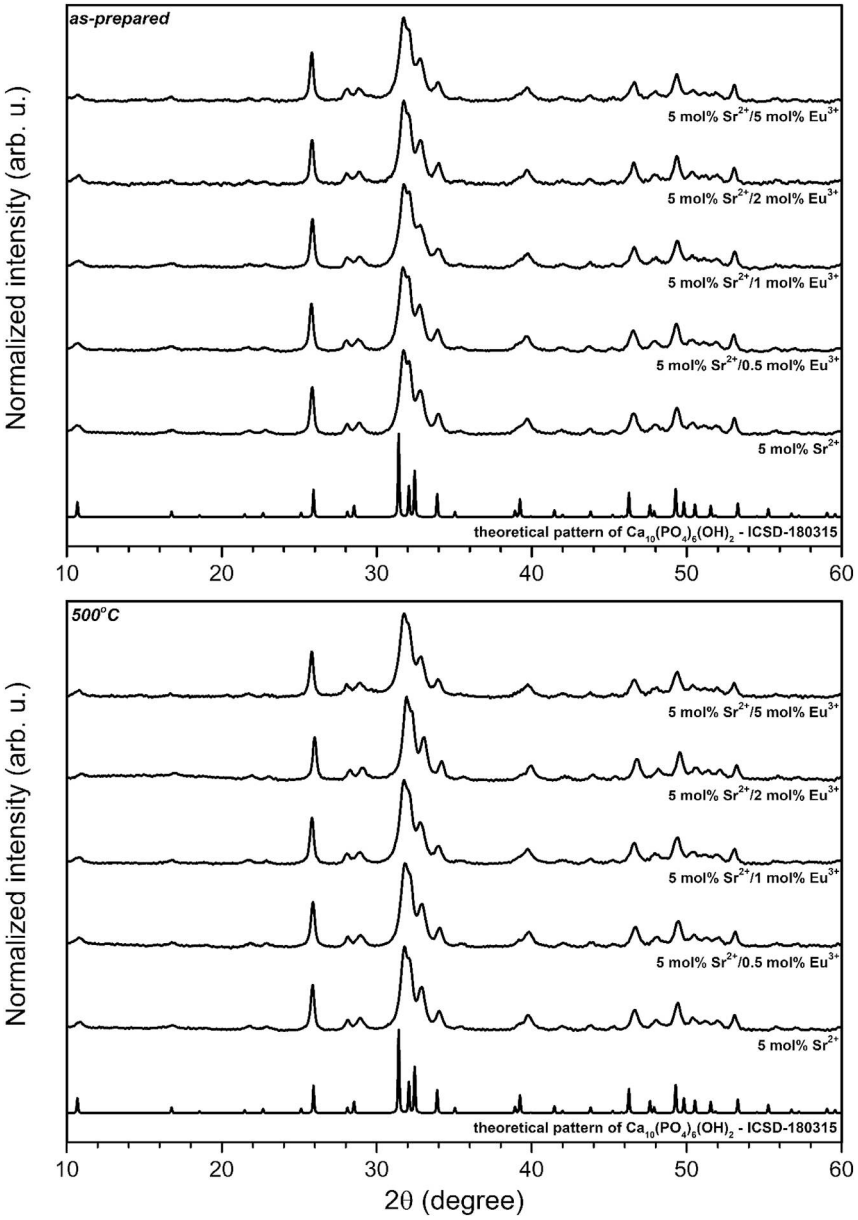

Fig. 1. X-ray powder diffraction patterns of the as-prepared (above) and annealed at 500 °C (below) Eu^{3+}/5 mol% Sr^{2+}:$Ca_{10}(PO_4)_6(OH)_2$ nanopowders compared to the theoretical pattern of hydroxyapatite (on the bottom of each figure) as a function of optically active ions concentration proving the crystal phase purity of obtained compounds.

3. Results and discussion

3.1. XRD and TEM analysis

The crystal characterization of the $Ca_{10}(PO_4)_6(OH)_2$ doped with Sr^{2+}, doped with Eu^{3+} and co-doped with 5 mol% Sr^{2+} and xEu^{3+} ions nanocrystals (where x = 0.5 mol%, 1 mol%, 2 mol%, 5 mol%) as-prepared and annealed at 500 °C was done by means of the powder XRD measurements (see Figs. 1 and S1). All the samples prepared by precipitation method and post-treated at 500 °C have shown only pure crystalline phases, corresponding to the reference standard of the hexagonal $Ca_{10}(PO_4)_6(OH)_2$ with space group $P6_3/m$ characteristic for the apatite family (ICSD-180315 [25]). Observed broadening of the diffraction peaks is connected with the coherent size of nanocrystalline particles. Materials were annealed also at 800 °C, but additional phase as β-$Ca_3(PO_4)_2$ was detected due to thermal decomposition caused by Sr^{2+} ions [20,27].

The structural refinement was calculated by using a Maud program version 2.68 [28,29] based on the apatite hexagonal crystal structure with better approximation and indexing of the Crystallographic Information File (CIF). The quality of structural refinement was checked by R-values (R_w, R_{wnb}, R_{all}, R_{nb}, and σ) which were applied to obtain a structural refinement with better quality and reliability. The hexagonal phase formation as well as the successful incorporation of Sr^{2+} and Eu^{3+} ions into the hydroxyapatite were confirmed. A good agreement between the observed XRD pattern and the theoretical fit indicating the success of the Rietveld refinement method is shown in Fig. S2 as a display of small differences near to zero on the intensity scale, as illustrated by a line ($Y_{Obs} - Y_{Calc}$). More details regarding Rietveld refinement are displayed in Tables 1 and 2. The projection of the hydroxyapatite co-doped with 2 mol% Eu^{3+} and 5 mol% Sr^{2+} unit cell and the coordination polyhedrals of Ca^{2+} cations are shown in Fig. 2. As can be seen in Table 1, it is only possible to observe a trend connected with an increase of average grain size caused by the temperature

Table 1
Unit cell parameters (*a*, *c*), cell volume (*V*), grain size as well as refine factor (R_w) for the Eu^{3+}/5 mol% Sr^{2+}:$Ca_{10}(PO_4)_6(OH)_2$ powder as function of Eu^{3+} ions concentration.

Sample	a (Å)	c (Å)	V (Å^3)	size (nm)	R_w (%)
Single crystal [25]	9.424(4)	6.879(4)	529.09(44)	–	–
As prepared					
Matrix	9.4218(1)	6.8744(3)	528.48(91)	12.0(1)	2.0
5 mol% Sr^{2+}	9.4463(5)	6.8958(2)	532.89(86)	17.2(1)	2.4
0.5 mol% Eu^{3+}	9.4550(3)	6.9021(0)	534.36(46)	12.0(3)	2.1
1 mol% Eu^{3+}	9.4433(4)	6.8899(1)	532.10(27)	11.0(2)	3.1
2 mol% Eu^{3+}	9.4554(3)	6.9034(3)	534.51(28)	17.0(0)	2.2
5 mol% Eu^{3+}	9.4486(8)	6.8979(8)	533.32(86)	12.0(3)	2.5
500 °C					
0.5 mol% Eu^{3+}	9.4197(7)	6.8863(3)	529.17(47)	25.0(2)	2.5
1 mol% Eu^{3+}	9.4392(4)	6.8955(2)	532.07(36)	22.0(2)	3.1
2 mol% Eu^{3+}	9.4059(7)	6.8788(5)	527.05(22)	25.1(0)	2.8
5 mol% Eu^{3+}	9.4375(9)	6.8981(2)	532.08(81)	20.0(1)	3.1

Table 2
Atomic parameters of the $Eu_{0.02}Sr_{0.05}Ca_{9.93}(PO_4)_6(OH)_2$.

Sample	$Ca_{10}(PO_4)_6(OH)_2$: 2 mol% Eu^{3+}/5 mol% Sr^{2+}; Z = 1
Space group	Hexagonal $P6_3/m$ (No. 176)
Calculated cell parameters	a = 9.4058(6) Å c = 6.8787(7) Å V = 527.03(37) Å^3
R_w	3.42%
R_{wnb}	3.07%
R_{all}	1.49%
R_{nb}	2.64%
σ	2.69%

Selected shortest contacts	
Ca|Sr|Eu – Ca|Sr|Eu	4.1983(2) Å
Ca|Sr|Eu – O	2.2106(1) Å
Ca|Sr|Eu – P	3.2973(3) Å
P – O	1.4961(1) Å
Ca|Sr|Eu – O – Eu|Sr|Ca	124.161(1)°

Atom	Wyckoff positions	x	y	z	B_{iso}	Occ. (< 1)
O1	6 h	0.3469	0.4750	0.25	0.0146906	
O2	6 h	0.5846	0.4595	0.25	0.0272043	
O3	12 i	0.3348	0.2414	0.0582	0.0909211	
P1	6 h	0.4025	0.3477	0.25	0.0225895	
Ca1	4 f	0.3324	0.6667	0.0074	0.0971982	0.9673
Ca2	6 h	0.2466	0.9822	0.25	0.0817034	0.9524
O4	4 e	0	0	0.1839	0.0713975	0.5
H1	4 e	0	0	0.0858	0.0352776	0.5
Sr1	4 f	0.3337	0.6664	0.0121	0.0662567	0.0277
Sr2	6 h	0.2576	0.9798	0.25	0.0978285	0.0326
Eu1	4 f	0.3334	0.6667	0.0075	0.0837738	0.0050
Eu2	6 h	0.2418	0.9718	0.25	0.0748735	0.0110

treatment. The average grain size of as-prepared materials is very low (11–17 nm) due to the high amount of amorphous phase present in these materials. After applying elevated temperature in the heat-treating process, the average grain size was growing until 20–26 nm at the expense of amorphous phase. The *a*, *c* and *V* cell parameters of obtained materials slightly decreased after thermal treatment, which is highly expected and well-known effect. Furthermore, there is no straightforward dopant concentration influence on the cell parameters or cell volume.

The morphology of the pure, 5 mol% Sr^{2+}-doped and 2 mol% Eu^{3+}/5 mol% Sr^{2+} co-doped calcium hydroxyapatite was studied using Transmission Electron Microscopy (TEM) and Selected Area Electron Diffraction (SAED) techniques. As can be seen in Fig. 3, nanoparticles are crystalline, aggregated and the shape of particles are irregular and elongated in one direction. The morphology of nanoparticles has not changed with the dopants substitution. The grain size has changed a little with dopants substitution. The particles size distributions of the studied systems were counted based on length and width diameters and presented as histograms. The size distributions are relatively wide. The average grain size of the pure, 5 mol% Sr^{2+}-doped and 2 mol% Eu^{3+}/5 mol% Sr^{2+} co-doped hydroxyapatite is about 9 nm in width and 33 nm in length, 11 nm × 39 nm and 13 nm × 31 nm, respectively. The preparation of pure hydroxyapatite phase was additionally confirmed by SAED analysis (inset).

The energy-dispersive X-ray spectrometer (EDS) as well as inductively coupled plasma (ICP) were applied to confirm the content of particular elements. The element maps were recorded by the scanning electron microscope equipped with an energy-dispersive X-ray spectrometer (SEM-EDAX) in order to check the elements incorporation frequency in the obtained material (Fig. 4). The results confirmed the established stoichiometry of dopants as well as the regular distribution of elements in the synthesized material.

The infrared spectra were measured for the pure, 5 mol% Sr^{2+}-doped and 2 mol% Eu^{3+}/5 mol% Sr^{2+} co-doped hydroxyapatite materials to investigate the functional groups present in materials and the dopants influence onto the apatite structure (see Fig. 5). The IR spectra consist of a typical vibrational bands of the phosphate PO_4^{3-} groups at 472.0 cm^{-1} (the doubly degenerate ν_2 bending); 564.6 cm^{-1}, 601.7 cm^{-1} and 632.0 cm^{-1} (the triply degenerate ν_4 vibration); 961.3 cm^{-1} (the ν_1 non-degenerate symmetric stretching); 1034.1 cm^{-1} and 1091.7 cm^{-1} (the triply degenerate ν_3 antisymmetric stretching). The vibrational transition at 3571 cm^{-1} belongs to stretching mode ($\nu(OH^-)$) and at 633 cm^{-1} and to librational mode ($L(OH)$) which obviously confirm the presence of the hydroxyl groups in the structure [30,31]. The transitions at 3431.9 cm^{-1} and 1637.3 cm^{-1} correspond to the H-O-H bands of lattice water. The ν_3 and ν_4 (PO_4^{3-}) vibration bands are the IR fingerprint of hydroxyapatite structure and their presence clearly confirms the purity of synthesized compounds [32]. Moreover, the obtained spectra are very similar to each other and only little differences between location of the maximum of peaks were observed.

3.2. Excitation and emission spectra

The excitation emission spectra of the obtained samples were measured at room temperature recording emission wavelength at 617 nm related to the most intense band of the $^5D_0 \rightarrow {}^7F_2$ electric dipole transition. All spectra were similar to each other without any significant differences, therefore only the representative excitation spectrum of as-prepared $Ca_{10}(PO_4)_6(OH)_2$:5 mol% Sr^{2+}/2 mol% Eu^{3+} was presented in Fig. 6. Sharp lines associated with the intraconfigurational *4f-4f* transitions characteristic for the Eu^{3+} ions as well as intense and broadband related to ligand-to-metal charge transfer (CT) $O^{2-} \rightarrow Eu^{3+}$ transition located in the UV range are present in excitation spectrum. Hence, the narrow lines observed at 299.3 nm (33,411 cm^{-1}) were attributed to the $^7F_0 \rightarrow {}^5F_{(4,3,2,1)}$, $^3P_0$ transitions, at 319.6 nm (31,289 cm^{-1}) to $^7F_0 \rightarrow {}^5H_{(6,5,4,7,3)}$, at 363.5 nm (27,510 cm^{-1}) to $^7F_0 \rightarrow {}^5D_4$, $^5L_8$ at 377.1 nm (26,518 cm^{-1}) to $^5L_8$, $^7F_0 \rightarrow G_2$, $^5L_7$, $^5G_3$, at 394.4 nm (25,355 cm^{-1}) to $^7F_0 \rightarrow {}^5L_6$, at 466 nm (21,459 cm^{-1}) to $^7F_0 \rightarrow {}^5D_2$ as well as at 527 nm (18,975 cm^{-1}) to $^7F_0 \rightarrow {}^5D_1$. Since the lanthanide's *f* orbitals are well isolated by external shell, the *f-f* electron transitions are weakly affected by the ligand field and the position of these peaks remains almost constant regardless of the host lattice structure. A different situation is observed in the case of the allowed CT transition, which is strongly affected by electron-lattice coupling and the peak position is depended on the ion's local symmetry. The CT maximum is located at 252.3 nm (39,635 cm^{-1}). As a matter of fact, the substitution of divalent Ca^{2+} by trivalent Eu^{3+} cations leads to the formation of cationic vacancies in the unit cell and the charge

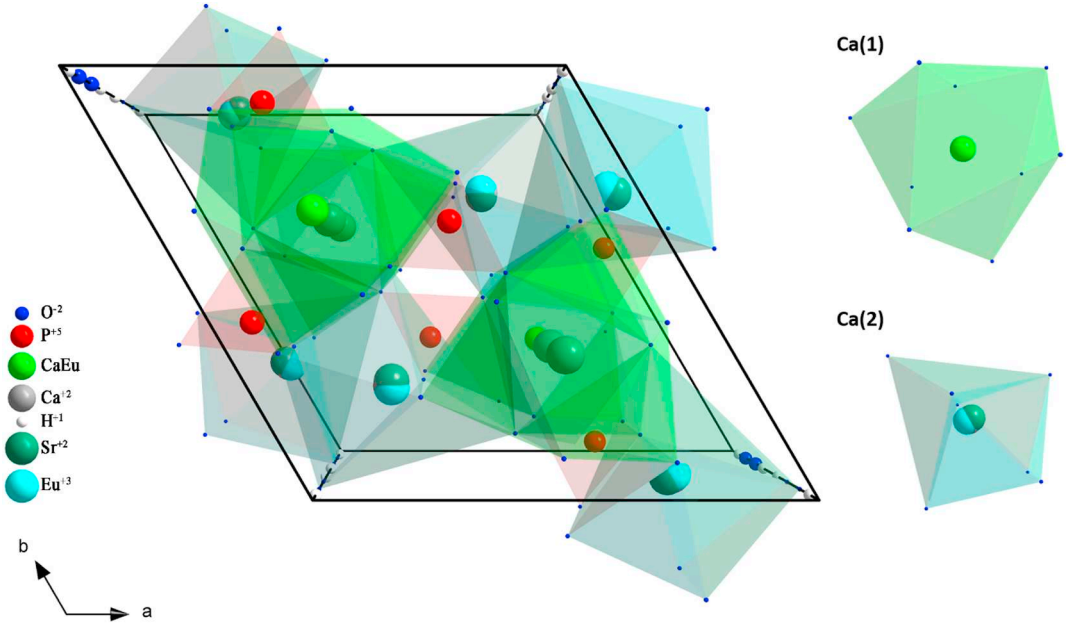

Fig. 2. The projection of the 2 mol% Eu^{3+}/5 mol% Sr^{2+}:$Ca_{10}(PO_4)_6(OH)_2$ unit cell and the coordination polyhedrals of Ca^{2+} cations.

compensation is required. Two mechanisms are well known and described previously in [8,20,33].

The emission spectra of as-prepared and annealed at 500 °C 5 mol% Sr^{2+}/*x* mol% Eu^{3+}:$Ca_{10}(PO_4)_6(OH)_2$ (where $x - 0.5 - 5$ mol%) materials were collected in the spectral range from 400 nm to 750 nm upon pulsed 266 nm excitation at 300 K as a function of optically active ions concentration (see Fig. 7). All of the spectra were normalized to the $^5D_0 \rightarrow {}^7F_1$ magnetic dipole transition. In general terms, the spectroscopic attitude of Eu^{3+} ions allows to get essential information about the symmetry of their immediate environment, the number of their crystallographic positions and therefore, potential sites of substitution, structural changes taking place in the matrix influenced by external factors [20]. Emission spectra of the trivalent europium ions consist of characteristic bands in the visible region of the electromagnetic radiation assign to the specific electron transitions occurring in the *4f-4f* shell of Eu^{3+} ions. In the analysis of the spectroscopic properties of Eu^{3+} ions, the $^5D_0 \rightarrow {}^7F_{0,1,2}$ transitions are the most important, particularly in correlation with structural properties [8,34].

In the case of as-prepared materials as well as annealed at 500 °C, the $^5D_0 \rightarrow {}^7F_0$ transition is split into three components located at 573.8 nm (17,428 cm^{-1}), 577.3 nm (17,322 cm^{-1}) and 579.2 nm (17,265 cm^{-1}). The Eu^{3+} ions are located at least into three different sites in this crystal structure. In hydroxyapatite lattice, there are two different kinds of crystallographic sites of Ca^{2+} ions: four at the Ca(1) site with C_3 symmetry, *4f* position which lies on the ternary axes and six at the Ca(2) site with C_s symmetry, *6h* position [35,36]. Additionally, *cis* and *trans* symmetry of the C_s crystallographic site related to arrangements of Eu^{3+} ions is well-known in the literature on apatite structures [27]. Furthermore, there is a charge incompatibility between Ca^{2+} and Eu^{3+} ions and ionic radii incompatibility (Ca^{2+} (CN9) = 1.18 Å, Eu^{3+} (CN9) = 1.12 Å, Ca^{2+} (CN7) = 1.06 Å, Eu^{3+} (CN7) = 1.01 Å) [37], which can lead to some variety of structural defects connected with the requirement of charge balance. Moreover, the Eu^{3+} polyhedral became more distorted after applying elevated temperature (see *R* value in Table 3). The substitution of divalent Ca^{2+} by trivalent Eu^{3+} cations leads to the formation of cationic vacancies in the lattice with the charge compensation effect described by Eq. (2). However, the first mechanism is much more likely in case of apatite and it is possible only for Ca(2) crystallographic site. The OH^- group is substituted by O^{2-} camming from atmospheric oxygen during annealing process.

$$Ca^{2+}(2) + OH^- \rightarrow Eu^{3+} + O^{2-}, \quad (1)$$

$$3Ca^{2+}(1) \rightarrow 2Eu^{3+} + V_{Ca(1)}. \quad (2)$$

The strontium substitution into calcium sites is also significant and leads to a change in the Eu^{3+} ions surrounding and consequently, to the appearance of additional lines of *0-0* transition. It is clearly visible that there is a difference between the intensity of particular components as well as the ratio between them. The emission of the Eu^{3+} ions from Ca (1) crystallographic site is the most intense compared with the Eu^{3+} emission from Ca(2) sites for as-synthesized materials. Initially, the Eu^{3+} ions preferentially substituted into Ca(1) position, which is well-known for as-synthesized apatite. The thermal diffusion of Eu^{3+} ions occurred from Ca(1) to Ca(2) sites after annealing process [27,38]. In annealed materials, the *0-0* transitions from Ca(2) sites are the most intense. It is in agreement with the charge compensation model, since the first mechanism (1) is much more probable. Moreover, the intensities of *0-0* transitions for materials annealed at 500 °C are stronger than for as-prepared materials. The abnormal high intensity of the $^5D_0 \rightarrow {}^7F_0$ transition can be caused by an increase of covalent character of the Eu^{3+}–O^{2-} bonding formed between the Eu^{3+} in Ca(2) position and O^{2-} ions created during charge compensation mechanisms to maintain the charge neutrality. The emission intensity from Eu(1) site could remain the same. Due to arising of the covalency of Eu^{3+}–O^{2-} bond in this material, the symmetry of the Ca(2) crystallographic site distorted from C_S to pseudo $C_{\infty V}$ symmetry. The $^5D_0 \rightarrow {}^7F_0$ transition is allowed and the $^5D_0 \rightarrow {}^7F_2$ transition is forbidden for this symmetry, what is manifesting in the relatively strong intensity of the $^5D_0 \rightarrow {}^7F_0$ transition [39].

The maximum of the $^5D_0 \rightarrow {}^7F_1$ transition is located at 590.5 nm (16,935 cm^{-1}). The band is split into five overlapping lines for as-prepared materials and even six lines for materials annealed at 500 °C. Depending on local symmetry of the Eu^{3+} ions, the $^7F_1$ multiplet could be split into three non-degenerate Stark components for each crystallographic with the low symmetry. However, at least three different sites in this matrix are occupied by Eu^{3+} ions, which is well-known in the literature. The most intense emission was observed for the hypersensitive $^5D_0 \rightarrow {}^7F_2$ transition in both cases. The barycentre of the $^5D_0 \rightarrow {}^7F_2$ transition is located at 616.5 nm (16,221 cm^{-1}) and is split

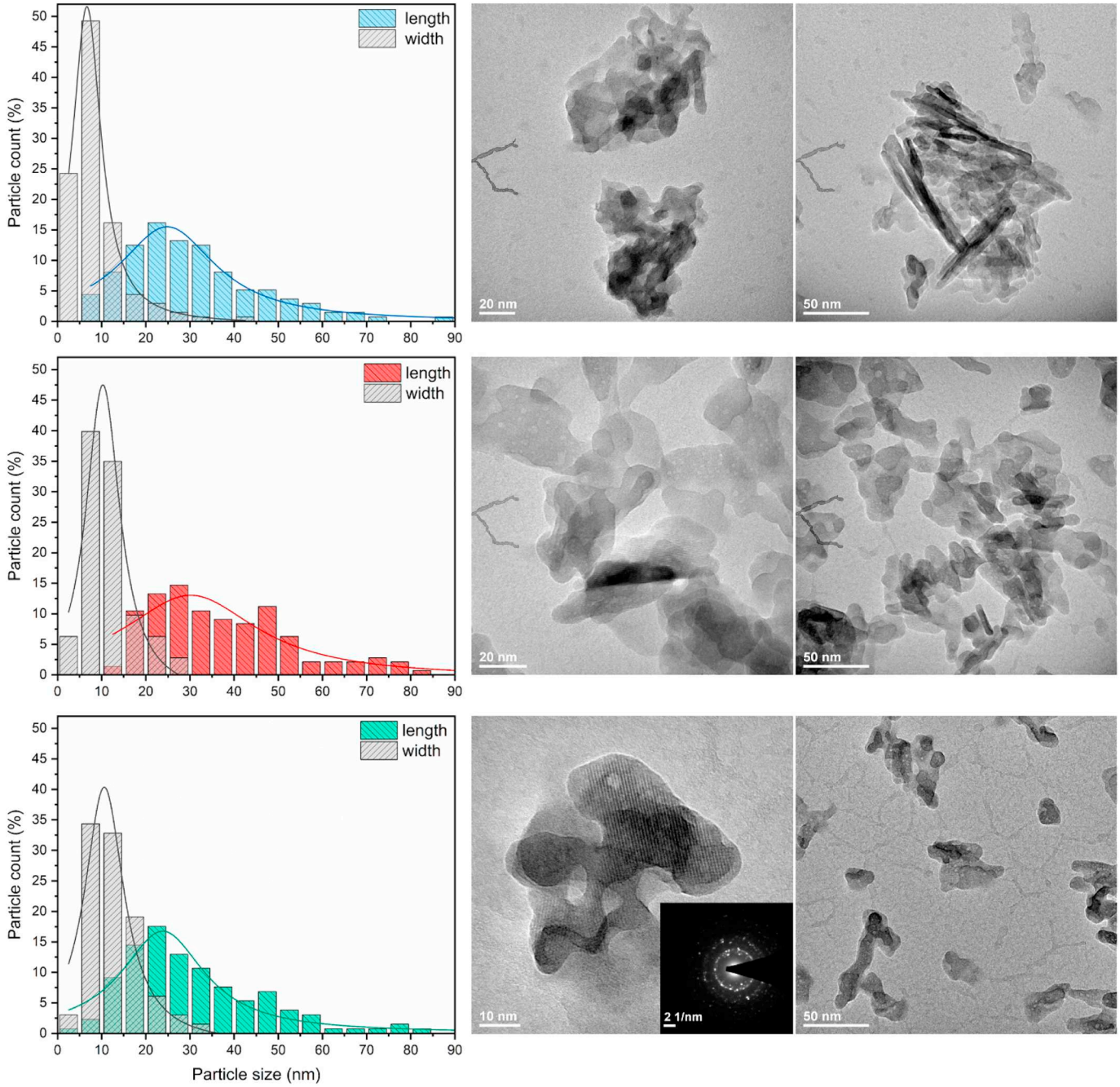

Fig. 3. The particle size distribution and the representative TEM images of the pure (upper), 5 mol% Sr^{2+}-doped (middle) and 2 mol% Eu^{3+}/5 mol% Sr^{2+} co-doped $Ca_{10}(PO_4)_6(OH)_2$ (bottom) as well as SAED image (inset).

into three overlapping lines in the case of as-prepared materials and into even six lines in the case of annealed at 500 °C materials. The maximum of the ${}^5D_0 \rightarrow {}^7F_3$ transition is located at 652.4 nm (15,328 cm^{-1}) and the ${}^5D_0 \rightarrow {}^7F_4$ band is around 701.1 nm (14,263 cm^{-1}). The most intense emission was observed in the case of the hypersensitive ${}^5D_0 \rightarrow {}^7F_2$ transition.

As a matter of fact, the intensity of the ${}^5D_0 \rightarrow {}^7F_2$ electric dipole transition is very sensitive to variations in the local surrounding of Eu^{3+} ions in the host lattice, whereas the intensity of the ${}^5D_0 \rightarrow {}^7F_1$ magnetic dipole transition is nearly independent of the crystal field influences. If the Eu^{3+} ion occupies a centrosymmetric site, the only permitted transition is the magnetic one. In opposite case, the electric dipole transition becomes dominant. The ratio of the relative emission intensities (R) is defined as follows:

$$R = \frac{\int {}^5D_0 \rightarrow {}^7F_2}{\int {}^5D_0 \rightarrow {}^7F_1} \quad (3)$$

In compliance with this factor, the ratio of the integral intensities of these transitions is needed to evaluate the asymmetry of the coordination polyhedron of Eu^{3+} ions and the variations in the local point symmetry. In the sequel, the higher the ratio between these transitions is, the less centrosymmetric is the local environment around Eu^{3+} ions. An impact of the annealing temperature and host lattice on the R-value is presented in Table 3. The R parameter increases with an increase of the annealing temperature, therefore the Eu^{3+} local environment became more distorted after post-heat treatment. Except that, no relationship between an increase of dopant concentration, neither in the

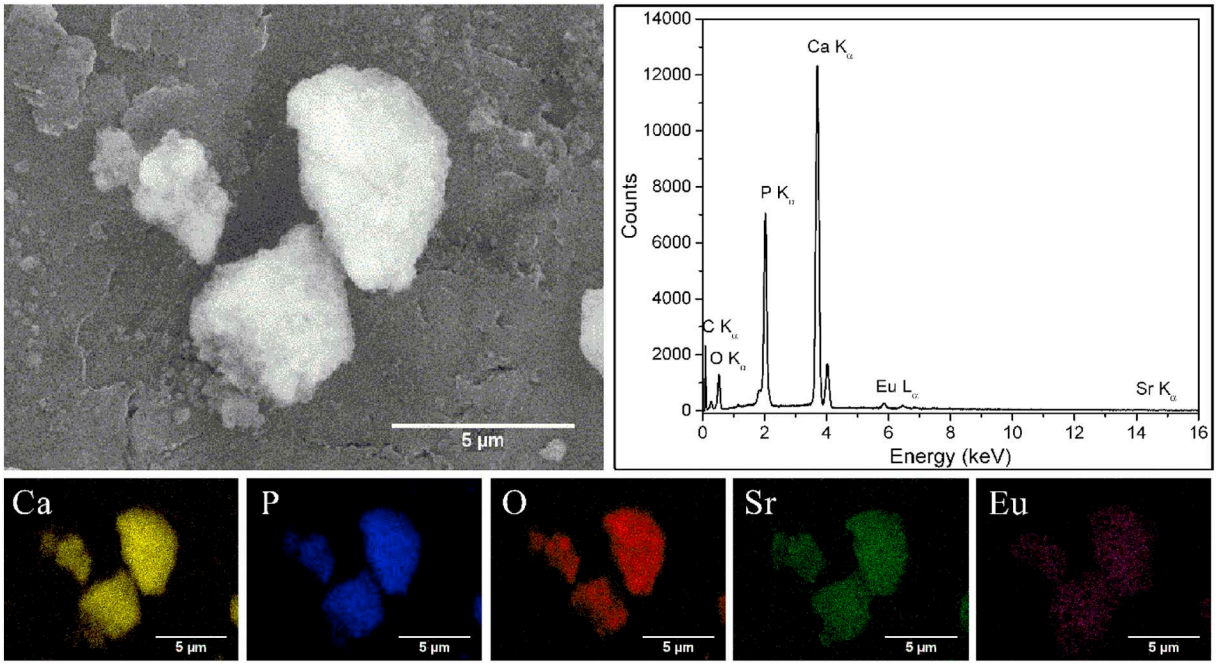

Fig. 4. SEM-EDS element maps and EDS spectrum of the 2 mol% Eu^{3+}/5 mol% Sr^{2+}:$Ca_{10}(PO_4)_6(OH)_2$ prepared by precipitation synthesis.

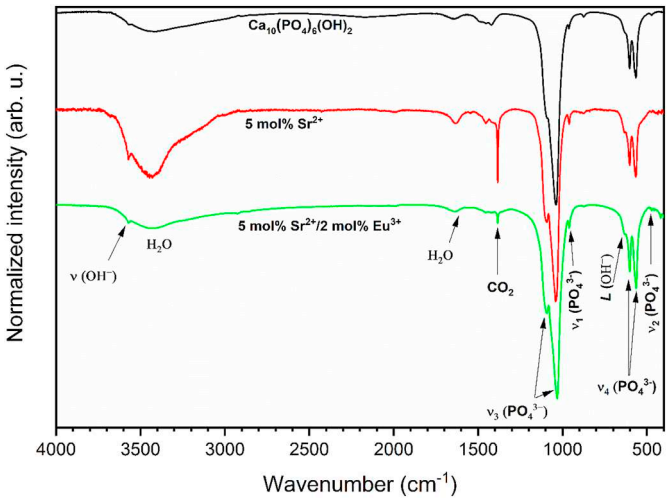

Fig. 5. IR spectra of the pure, 5 mol% Sr^{2+}-doped and 2 mol% Eu^{3+}/5 mol% Sr^{2+} co-doped $Ca_{10}(PO_4)_6(OH)_2$ with the vibrations assigned.

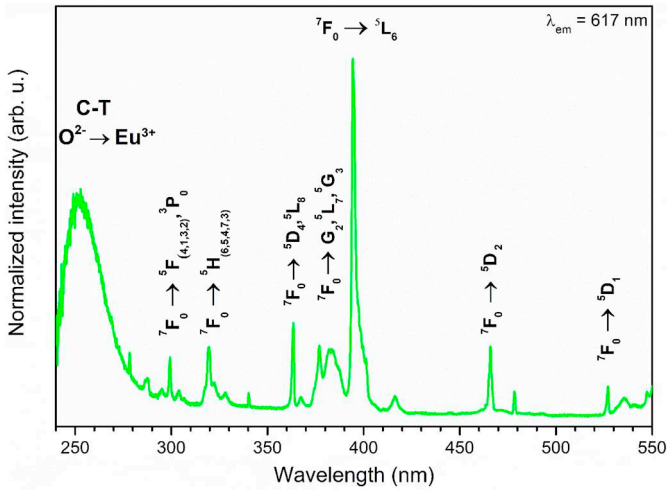

Fig. 6. Representative excitation emission spectra of the as-prepared 2 mol% Eu^{3+}/5 mol% Sr^{2+}:$Ca_{10}(PO_4)_6(OH)_2$ with the Eu^{3+} transitions assigned.

case of as-prepared materials nor heat-treated, was observed. The *R*-values behave incalculably in those cases.

The simplified Judd–Ofelt theory was applied to state the intensity parameters Ω_2 and Ω_4. The outcomes of this approach are listed in Table 3. It is worth noting that the value of the Ω_2 parameter slightly changes with an increase of the Eu^{3+} ions concentration, but it is impossible to find any tendency. However, there is a possibility to note that the value of Ω_2 parameter increased in the annealed materials what indicate an increase in the distortion of Eu^{3+} coordination polyhedra and could be related to an increase of the covalence character of the Eu^{3+}–O^{2-} bond. The Ω_4 value provides some information about changes in the electron density around Eu^{3+} cations. However, the value of Ω_4 cannot be straight connected with the Eu^{3+} ions symmetry changes, but can give some information about the electron density variations of the O^{2-} anions surrounding influencing on the position of the CT band.

3.3. Decay times

With the aim of determining the comprehensive characteristics of the luminescence properties, the luminescence kinetics were analyzed for all synthesized materials. The room temperature decay times corresponding to the $^5D_0 \rightarrow {}^7F_2$ transition were measured and monitored at the wavelength of 618 nm. The samples were excited by pulse radiation of 266 nm and the luminescence kinetics curves are shown in Fig. 8. The decay profiles are not single-exponential in all cases and the physical meaning of multi-exponential fitting is complicated to explain, hence the lifetime values were calculated from the effective emission decay times by using the following equation:

$$\tau_m = \frac{\int_0^{\infty} tI(t)dt}{\int_0^{\infty} I(t)dt} \cong \frac{\int_0^{t^{max}} tI(t)dt}{\int_0^{t^{max}} I(t)dt} \quad (4)$$

where $I(t)$ is the luminescence intensity at time t corrected for the

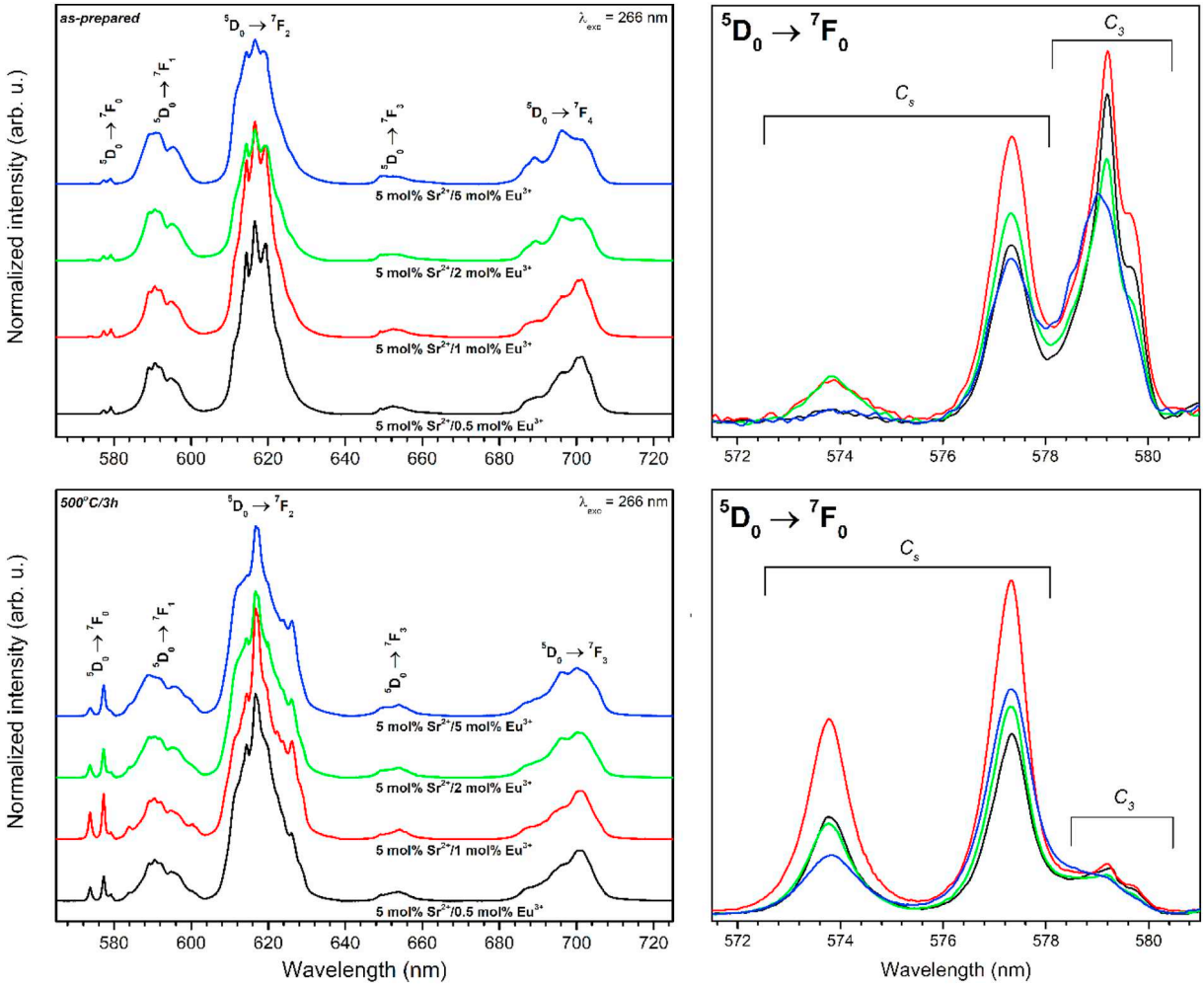

Fig. 7. Emission spectra of the as-prepared (above) and annealed at 500 °C (below) Eu^{3+}/5 mol% Sr^{2+}:$Ca_{10}(PO_4)_6(OH)_2$ as a function of optically active ions concentration with the Eu^{3+} transitions assigned.

background and the integrals are calculated over the range of $0 < t < t_{max}$, where $t_{max} \gg \tau_m$.

The decay profiles, as well as the lifetime values, are similar to each other and only little changes were observed. The decay curves of as-prepared materials are more non-exponential and the value of decay times are shorter than for heat-treated materials, what could be connected with higher grain size for annealed materials and consequently, lower volume to surface ratio. Generally, the lifetime values decrease with increase of the Eu^{3+} concentration in both cases as-prepared and heat-treated materials.

3.4. Antibacterial properties of Eu^{3+}/Sr^{2+}: $Ca_{10}(PO_4)_6(OH)_2$ nanopowders

Despite the common practice of preoperative antimicrobial prophylaxis with antibiotics and a high level of attentiveness of aseptic condition in operating rooms, the infections after medical procedures are still about 30% of cases. Therefore, the antibacterial activity of implants should be considered at the stage of designing new bioactive materials. Implantation of bones with modified hydroxyapatites with improved biocompatibility and antibacterial effect can influence the healing process and the patient comfort during the treatment

Table 3
Decay rates of radiative (A_{rad}), non-radiative (A_{nrad}) and total (A_{tot}) processes of $^5D_0 \rightarrow {}^7F_J$ transitions, luminescence lifetimes (τ), intensity parameters (Ω_2, Ω_4), quantum efficiency (η) and asymmetry ratio (R) of the as-prepared and annealed materials.

Sample	A_{rad} (s^{-1})	A_{nrad} (s^{-1})	A_{tot} (s^{-1})	T (ms)	Ω_2 (10^{-20} cm^2)	Ω_4 (10^{-20} cm^2)	η (%)	R
As-prepared								
0.5 mol% Eu^{3+}	249.34	383.57	632.91	1.58	5.6101	4.6951	39.40	3.988
1 mol% Eu^{3+}	268.10	349.18	617.28	1.62	6.3085	4.6823	43.43	4.485
2 mol% Eu^{3+}	195.19	534.74	729.93	1.37	3.9704	3.9444	26.74	2.823
5 mol% Eu^{3+}	219.21	635.49	854.70	1.17	4.5540	4.5775	25.65	3.238
500 °C								
0.5 mol% Eu^{3+}	311.57	162.37	473.94	2.11	7.7557	5.0110	65.74	5.514
1 mol% Eu^{3+}	307.19	183.01	490.20	2.04	7.8770	4.4197	62.67	5.600
2 mol% Eu^{3+}	276.55	275.94	552.49	1.81	6.7177	4.4788	50.05	4.776
5 mol% Eu^{3+}	283.02	291.69	574.71	1.74	6.8505	4.7009	49.25	4.870

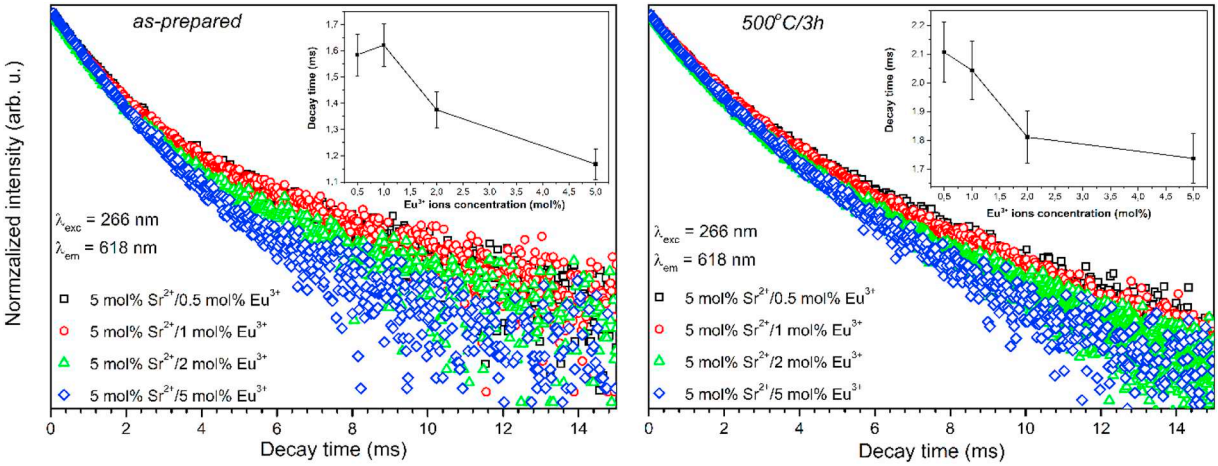

Fig. 8. Decay times of the as-prepared (left) and annealed at 500 °C (right) Eu^{3+}/5 mol% Sr^{2+}:$Ca_{10}(PO_4)_6(OH)_2$ as a function of optically active ions concentration. The dependence of decay times on the Eu^{3+} ions concentration as insets in each figure.

procedure. Recently Tite et al. analyzed different cationic substitutions in hydroxyapatites that have been reported in literature up to date. Amongst plethora of different cations, europium and strontium were reported to possess antibacterial effect depending on tested concentrations and mol% ratio of dopant in the biomaterial [23].

In presented study, six different materials were chosen to demonstrate their antimicrobial potential: $Ca_{10}(PO_4)_6(OH)_2$ doped with Eu^{3+} at 2 or 5 mol% ratio (2 mol% Eu^{3+} and 5 mol% Eu^{3+}), $Ca_{10}(PO_4)_6(OH)_2$ doped with Sr^{2+} at 2 or 5 mol% ratio (2 mol% Sr^{2+} and 5 mol% Sr^{2+}) and $Ca_{10}(PO_4)_6(OH)_2$ co-doped with Eu^{3+} and Sr^{2+} at 2 or 5 mol% ratio (2 mol% Eu^{3+} and 2 mol% Sr^{2+} as well as 5 mol% Eu^{3+} and 5 mol% Sr^{2+}), respectively. For antibacterial properties testing, we decided to choose different amounts of dopants alone and in doublet to check their synergistic/antagonistic effect in designed biomaterials.

The hydroxyapatite nanopowders were first screened at a range of concentrations (1, 10 and 100 μg/mL) and 100 μg/mL concentration was chosen for further tests. The antimicrobial effect was presented as a bacterial colony count (log from CFU/mL) variation in comparison to the control untreated culture (Fig. 9).

Considering the antimicrobial activity of tested biomaterials the differences of 0.5-log reduction or increase in the bacterial count were observed. Nevertheless, such differences should be considered as non-significant from a microbiological point of view. Thus we could conclude that europium and strontium co-doped hydroxyapatites are neutral to tested bacteria.

Strontium as a dopant is mainly treated as an agent that improves biocompatibility of apatites stimulating bone formation [23]. We may find papers showing a strong antibacterial effect of strontium ranelate-loaded poly(lactic-*co*-glycolic) acid microspheres assembled with Ag nanoparticles and hydroxyapatite nanoparticles against Gram-positive pathogen *Staphylococcus aureus* [40]. We demonstrate here that this ion has no antibacterial effect if prepared as co-doped hydroxyapatites. Europium alone doped nanopowders did not have antibacterial effect on *E. coli* which is consistent with previous report by Iconaru et al. [41] and Wiglusz et al. [26]. Unfortunately, the combination of both ions (strontium and europium) had no improved antibacterial effect compared to single ion-doped apatites. Similar dual ionic substitutions with strontium and cerium in hydroxyapatite have been already reported by Gopi et al. [42] and conversely, the authors noticed an antibacterial effect against *S. aureus* and *E. coli*.

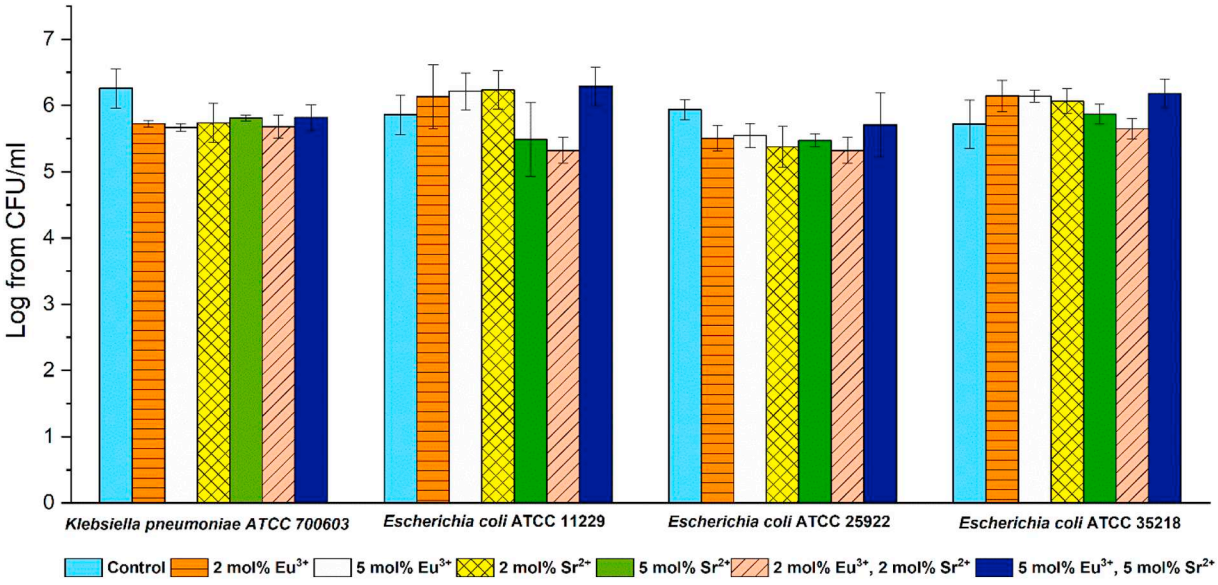

Fig. 9. Antibacterial effect of tested $Ca_{10}(PO_4)_6(OH)_2$ un-doped, doped or co-doped with Eu^{3+} and Sr^{2+} at the colloidal suspension of 100 μg/mL in saline against *Klebsiella pneumoniae* ATCC 700603, *Escherichia coli* ATCC 11229, *Escherichia coli* ATCC 25922 and *Escherichia coli* ATCC 35218. Controls consist of bacteria inoculated in saline; mean ± SD, $n = 3$.

4. Conclusion

A precipitation method was successfully applied to synthesized nanopowders of the hexagonal calcium hydroxyapatite co-doped with xEu^{3+} (where x = 0.5, 1, 2, 5 mol%) and 5 mol% Sr^{2+}. The structural and luminescence properties were investigated in detail for as-prepared as well as annealed at 500 °C materials. The pure hexagonal structure and the successful incorporation of the Eu^{3+} ions into the apatite lattice were confirmed by the XRD analysis. The nanometric size of synthesized apatite powders was confirmed by Rietveld calculations and TEM microscopy. In the presented materials, the Eu^{3+} ions occupied three possible crystallographic sites revealed in emission spectra: one Ca(1) site with C_3 symmetry and two Ca(2) sites with C_s symmetry arranged as *cis* and *trans* symmetry in this lattice. In the case of as-prepared materials, the Eu^{3+} ions occupied mainly Ca(1), but in the case of annealed materials, Eu^{3+} ions occupied mainly Ca(2) site. Moreover, the $^5D_0 \rightarrow {}^7F_0$ transition shown the abnormal strong intensity for annealed materials connected with the increase of covalency character of the Eu^{3+}–O^{2-} bond, which arises as an effect of the charge compensation mechanism. A simplified Judd–Ofelt theory in connection with the spectroscopic properties was employed and analyzed. The change in the R parameter yield the same trend as Ω_2 parameter implied an increase in the distortion of the europium coordination polyhedra and the Eu^{3+}–O^{2-} bond becomes more covalent. The average lifetimes of as-prepared materials are shorter than for annealed materials what is connected with higher grain size in the case of annealed materials and consequently, lower volume to surface ratio. The lifetime values decrease with an increase of Eu^{3+} ions concentration in as-prepared and annealed materials.

The hydroxyapatite nanopowders doped with Eu^{3+} and Sr^{2+} ions can improve bone formation as well as can enable bioimaging, but do not have antibacterial properties. Nevertheless, such preparations can be used as a theranostic agent come up to both functions: therapy and diagnosis.

Declaration of competing interest

The authors declare that they have no known competing financial interests or personal relationships that could have appeared to influence the work reported in this paper.

Acknowledgments

The authors would like to acknowledge from National Science Centre for financial support (no. UMO-2012/05/E/ST5/03904 and no. UMO-2015/19/B/ST5/01330). Katarzyna Szyszka received financial resources within the confines of financing the ETIUDA doctoral scholarship from the National Science Centre, Poland (no. UMO-2016/20/T/ST5/00493). Michael Giersig thanks Guangdong Innovative and Entrepreneurial Research Team Program China. titled “Plasmonic Nanomaterials and Quantum Dots for Light Management in Optoelectronic Devices” (no. 2016ZT06C517) for financial support. We are grateful for XRD measurements to M.Sc. E. Bukowska, for SEM images to Ph.D. D. Szymanski and for IR spectra to Ph.D. A. Ciupa-Litwa.

Appendix A. Supplementary data

Supplementary data to this article can be found online at https://doi.org/10.1016/j.jinorgbio.2019.110884.

References

[1] N. Neves, B.B. Campos, I.F. Almeida, P.C. Costa, A.T. Cabral, M.A. Barbosa, C.C. Ribeiro, Strontium-rich injectable hybrid system for bone regeneration, Mater. Sci. Eng. C. 59 (2016) 818–827, https://doi.org/10.1016/j.msec.2015.10.038.

[2] M. Schumacher, A. Lode, A. Helth, M. Gelinsky, A novel strontium(II)-modified calcium phosphate bone cement stimulates human-bone-marrow-derived mesenchymal stem cell proliferation and osteogenic differentiation in vitro, Acta Biomater. 9 (2013) 9547–9557, https://doi.org/10.1016/j.actbio.2013.07.027.

[3] F.M. Chen, X. Liu, Advancing biomaterials of human origin for tissue engineering, Prog. Polym. Sci. 53 (2016) 86–168, https://doi.org/10.1016/j.progpolymsci.2015.02.004.

[4] K. Lin, P. Liu, L. Wei, Z. Zou, W. Zhang, Y. Qian, Y. Shen, J. Chang, Strontium substituted hydroxyapatite porous microspheres: surfactant-free hydrothermal synthesis, enhanced biological response and sustained drug release, Chem. Eng. J. 222 (2013) 49–59, https://doi.org/10.1016/j.cej.2013.02.037.

[5] Y. Huang, M. Hao, X. Nian, H. Qiao, X. Zhang, X. Zhang, G. Song, J. Guo, X. Pang, H. Zhang, Strontium and copper co-substituted hydroxyapatite-based coatings with improved antibacterial activity and cytocompatibility fabricated by electrodeposition, Ceram. Int. 42 (2016) 11876–11888, https://doi.org/10.1016/j.ceramint.2016.04.110.

[6] B. Parekh, M. Joshi, A. Vaidya, Characterization and inhibitive study of gel-grown hydroxyapatite crystals at physiological temperature, J. Cryst. Growth 310 (2008) 1749–1753, https://doi.org/10.1016/j.jcrysgro.2007.11.219.

[7] M.H. Fathi, A. Hanifi, V. Mortazavi, Preparation and bioactivity evaluation of bone-like hydroxyapatite nanopowder, J. Mater. Process. Technol. 202 (2008) 536–542, https://doi.org/10.1016/j.jmatprotec.2007.10.004.

[8] K. Zawisza, P. Sobierajska, G. Renaudin, J.-M. Nedelec, R.J. Wiglusz, Effects of crystalline growth on structural and luminescence properties of $Ca_{(10-3x)}Eu_{2x}(PO_4)_6F_2$ nanoparticles fabricated by using a microwave driven hydrothermal process, CrystEngComm 19 (2017) 6936–6949, https://doi.org/10.1039/C7CE01454F.

[9] P. Sobierajska, A. Dorotkiewicz-Jach, K. Zawisza, J. Okal, T. Olszak, Z. Drulis-Kawa, R.J. Wiglusz, Preparation and antimicrobial activity of the porous hydroxyapatite nanoceramics, J. Alloys Compd. 748 (2018) 179–187, https://doi.org/10.1016/j.jallcom.2018.03.162.

[10] M. Sadat-Shojai, M.-T. Khorasani, E. Dinpanah-Khoshdargi, A. Jamshidi, Synthesis methods for nanosized hydroxyapatite with diverse structures, Acta Biomater. 9 (2013) 7591–7621, https://doi.org/10.1016/j.actbio.2013.04.012.

[11] X. Liu, P.K. Chu, C. Ding, Surface nano-functionalization of biomaterials, Mater. Sci. Eng. R 70 (2010) 275–302, https://doi.org/10.1016/j.mser.2010.06.013.

[12] M. Sadat-Shojai, Preparation of hydroxyapatite nanoparticles: comparison between hydrothermal and solvo-treatment processes and colloidal stability of produced nanoparticles in a dilute experimental dental adhesive, J. Iran. Chem. Soc. 6 (2009) 386–392, https://doi.org/10.1007/BF03245848.

[13] C. Shi, J. Gao, M. Wang, J. Fu, D. Wang, Y. Zhu, Ultra-trace silver-doped hydroxyapatite with non-cytotoxicity and effective antibacterial activity, Mater. Sci. Eng. C. 55 (2015) 497–505, https://doi.org/10.1016/j.msec.2015.05.078.

[14] J. Gao, M. Wang, C. Shi, L. Wang, Y. Zhu, D. Wang, A facile green synthesis of trace Si, Sr and F multi-doped hydroxyapatite with enhanced biocompatibility and osteoconduction, Mater. Lett. 196 (2017) 406–409, https://doi.org/10.1016/j.matlet.2017.03.054.

[15] S. Lala, T.N. Maity, M. Singha, K. Biswas, S.K. Pradhan, Effect of doping (Mg, Mn, Zn) on the microstructure and mechanical properties of spark plasma sintered hydroxyapatites synthesized by mechanical alloying, Ceram. Int. 43 (2017) 2389–2397, https://doi.org/10.1016/j.ceramint.2016.11.027.

[16] M. Schumache, A. Henß, M. Rohnke, M. Gelinsky, A novel and easy-to-prepare strontium(II) modified calcium phosphate bone cement with enhanced mechanical properties, Acta Biomater. 9 (2013) 7536–7544, https://doi.org/10.1016/j.actbio.2013.03.014.

[17] O. Kaygili, S. Keser, M. Kom, Y. Eroksuz, S.V. Dorozhkin, T. Ates, I.H. Ozercan, C. Tatar, F. Yakuphanoglu, Strontium substituted hydroxyapatites: synthesis and determination of their structural properties, in vitro and in vivo performance, Mater. Sci. Eng. C. 55 (2015) 538–546, https://doi.org/10.1016/j.msec.2015.05.081.

[18] E. Landi, A. Tampieri, G. Celotti, S. Sprio, M. Sandri, G. Logroscino, Sr-substituted hydroxyapatites for osteoporotic bone replacement, Acta Biomater. 3 (2007) 961–969, https://doi.org/10.1016/j.actbio.2007.05.006.

[19] U. Patel, R.M. Moss, K.M.Z. Hossain, A.R. Kennedy, E.R. Barney, I. Ahmed, A.C. Hannon, Structural and physico-chemical analysis of calcium/strontium substituted, near-invert phosphate based glasses for biomedical applications, Acta Biomater. 60 (2017) 109–127, https://doi.org/10.1016/j.actbio.2017.07.002.

[20] K. Zawisza, R.J. Wiglusz, Preferential site occupancy of Eu^{3+} ions in strontium hydroxyapatite nanocrystalline – $Sr_{10}(PO_4)_6(OH)_2$ – structural and spectroscopic characterisation, Dalt. Trans. 46 (2017) 3265–3275, https://doi.org/10.1039/C6DT04731A.

[21] A. Przekora, Current trends in fabrication of biomaterials for bone and cartilage regeneration: materials modifications and biophysical stimulations, Int. J. Mol. Sci. 20 (2019) 435, https://doi.org/10.3390/ijms20020435.

[22] D.R. Giacobbe, M. Mikulska, C. Viscoli, Recent advances in the pharmacological management of infections due to multidrug-resistant Gram-negative bacteria, Expert. Rev. Clin. Pharmacol. 11 (2018) 1219–1236, https://doi.org/10.1080/17512433.2018.1549487.

[23] T. Tite, A.-C. Popa, L.M. Balescu, I.M. Bogdan, I. Pasuk, J.M.F. Ferreira, G.E. Stan, Cationic substitutions in hydroxyapatite: current status of the derived biofunctional effects and their in vitro interrogation methods, Materials (Basel) 11 (2018) 2081, https://doi.org/10.3390/ma11112081.

[24] L. Sundarabharathi, H. Parangusan, D. Ponnamma, M.A.A. Al-maadeed, M. Chinnaswamy, In-vitro biocompatibility, bioactivity and photoluminescence properties of Eu^{3+}/Sr^{2+} dual-doped nano-hydroxyapatite for biomedical applications, J. Biomed. Mater. Res. - Part B Appl. Biomater. 106 (2018) 2190–2201,

https://doi.org/10.1002/jbm.b.34023.
[25] E. Balan, S. Delattre, D. Roche, L. Segalen, G. Morin, M. Guillaumet, M. Blanchard, M. Lazzeri, C. Brouder, E.K.H. Salje, Line-broadening effects in the powder infrared spectrum of apatite, Phys. Chem. Miner. 38 (2011) 111–122, https://doi.org/10.1007/s00269-010-0388-x.
[26] R.J. Wiglusz, Z. Drulis-Kawa, R. Pazik, K. Zawisza, A. Dorotkiewicz-Jach, J. Roszkowiak, J.-M. Nedelec, Multifunctional lanthanide and silver ion co-doped nano-chlorapatites with combined spectroscopic and antimicrobial properties, Dalton Trans. 44 (2015) 6918–6925, https://doi.org/10.1039/C5DT00046G.
[27] K. Zawisza, A. Strzep, R.J. Wiglusz, Influence of annealing temperature on the spectroscopic properties of hydroxyapatite analogues doped with Eu^{3+}, New J. Chem. 41 (2017) 9990–9999, https://doi.org/10.1039/C7NJ01380A.
[28] H.M. Rietveld, A profile refinement method for nuclear and magnetic structures, J. Appl. Crystallogr. 2 (1969) 65–71, https://doi.org/10.1107/S0021889869006558.
[29] L. Lutterotti, S. Matthies, H.-R. Wenk, MAUD: a friendly Java program for material analysis using diffraction, IUCr Newsl. CPD. 21 (1999) 14–15, https://doi.org/10.1007/BF02074985.
[30] J.R. Guerra-López, G.A. Echeverría, J.A. Güida, R. Viña, G. Punte, Synthetic hydroxyapatites doped with Zn(II) studied by X-ray diffraction, infrared, Raman and thermal analysis, J. Phys. Chem. Solids 81 (2015) 57–65, https://doi.org/10.1016/j.jpcs.2015.01.017.
[31] Q. Yuan, J. Wu, C. Qin, A. Xu, Z. Zhang, S. Lin, X. Ren, P. Zhang, Spin-coating synthesis and characterization of Zn-doped hydroxyapatite/polylactic acid composite coatings, Surf. Coatings Technol. 307 (2016) 461–469, https://doi.org/10.1016/j.surfcoat.2016.09.021.
[32] Y. Huang, H. Qiao, X. Nian, X. Zhang, X. Zhang, G. Song, Z. Xu, H. Zhang, S. Han, Improving the bioactivity and corrosion resistance properties of electrodeposited hydroxyapatite coating by dual doping of bivalent strontium and manganese ion, Surf. Coatings Technol. 291 (2016) 205–215, https://doi.org/10.1016/j.surfcoat.2016.02.042.
[33] P. Sobierajska, R. Pazik, K. Zawisza, G. Renaudin, J.-M. Nedelec, R.J. Wiglusz, Effect of lithium substitution on the charge compensation, structural and luminescence properties of nanocrystalline $Ca_{10}(PO_4)_6F_2$ activated with Eu^{3+} ions, CrystEngComm 18 (2016) 3447–3455, https://doi.org/10.1039/C6CE00320F.
[34] S. Targonska, K. Szyszka, J. Rewak-Soroczynska, R.J. Wiglusz, A new approach to spectroscopic and structural studies of the nano-sized silicate-substituted hydroxyapatite doped with Eu^{3+} ions, Dalt. Trans. 48 (2019) 8303–8316, https://doi.org/10.1039/c9dt01025d.
[35] B. Badraoui, A. Bigi, M. Debbabi, M. Gazzano, N. Roveri, R. Thouvenot, Physicochemical properties and structural refinement of strontium-lead hydroxyapatites, Eur. J. Inorg. Chem. 2002 (2002) 1864–1870.
[36] Y. Han, X. Wang, H. Dai, S. Li, Synthesis and luminescence of Eu^{3+} doped hydroxyapatite nanocrystallines: effects of calcinations and Eu^{3+} content, J. Lumin. 135 (2013) 281–287, https://doi.org/10.1016/j.jlumin.2012.09.029.
[37] R.D. Shannon, Revised effective ionic radii and systematic studies of interatomic distances in halides and chalcogenides, Acta Crystallogr. A 32 (1976) 751–767, https://doi.org/10.1107/S0567739476001551.
[38] P. Martin, G. Carlot, A. Chevarier, C. Den-Auwer, G. Panczer, Mechanisms involved in thermal diffusion of rare earth elements in apatite, J. Nucl. Mater. 275 (1999) 268–276.
[39] R. Ternane, M. Trabelsi-Ayedi, N. Kbir-Ariguib, B. Piriou, Luminescent properties of Eu^{3+} in calcium hydroxyapatite, J. Lumin. 81 (1999) 165–170.
[40] Z. Mao, Y. Li, Y. Yang, Z. Fang, X. Chen, Y. Wang, J. Kang, X. Qu, W. Yuan, K. Dai, B. Yue, Osteoinductivity and antibacterial properties of strontium ranelate-loaded poly(lactic-co-glycolic acid) microspheres with assembled silver and hydroxyapatite nanoparticles, Front. Pharmacol. 9 (2018) 368, https://doi.org/10.3389/fphar.2018.00368.
[41] S. Iconaru, M. Motelica-heino, D. Predoi, Study on europium-doped hydroxyapatite nanoparticles by Fourier transform infrared spectroscopy and their antimicrobial properties, 2013 (2013), https://doi.org/10.1155/2013/284285.
[42] D. Gopi, S. Ramya, D. Rajeswari, P. Karthikeyan, L. Kavitha, Strontium, cerium co-substituted hydroxyapatite nanoparticles: synthesis, characterization, antibacterial activity towards prokaryotic strains and in vitro studies, Colloids Surfaces A Physicochem. Eng. Asp. 451 (2014) 172–180, https://doi.org/10.1016/j.colsurfa.2014.03.035.